Available online at www.sciencedirect.com
ScienceDirect
Ocean Modelling 15 (2006) 56–70
Ocean Modelling
www.elsevier.com/locate/ocemod

To continue or discontinue: Comparisons of continuous and discontinuous Galerkin formulations in a spectral element ocean model

J.C. Levin [a,*], M. Iskandarani [b], D.B. Haidvogel [a]

[a] Institute of Marine and Coastal Sciences, Rutgers University, 71 Dudley Road, New Brunswick, NJ 08901, USA
[b] Rosenstiel School of Marine and Atmospheric Science, University of Miami, 4600 Rickenbacker Causeway, Miami, FL 33149, USA

Received 14 March 2005; received in revised form 15 September 2005; accepted 13 October 2005
Available online 9 November 2005

Abstract

The discontinuous Galerkin method is implemented in the spectral element ocean model to replace a continuous Galerkin discretization of the continuity and the tracer evolution equations. The aim is to improve the model's local conservation properties, and thus its performance in advection-dominated flows. The new model is validated against several oceanic benchmark problems, particularly ones that feature frontal structures and under-resolved features. Comparisons confirm the advantages of the DGM, including enhanced model robustness.

Keywords: Discontinuous Galerkin method; Spectral element method; Oceanic simulation; Shallow water equations; Ocean model

1. Introduction

The simulation of large scale geophysical flows raises a number of challenging computational problems associated with the representation of advection-dominated, rotating and stratified flows in thin fluid layers with steep topographic slopes (Willebrand and Haidvogel, 2001). The new generation of finite-difference-based ocean models have successfully addressed some of these issues which, along with the growth of available computational resources, has led to substantial improvements in performance. Most notable are the improvements to the models' advection schemes which are now locally conservative, upstream-biased (and generally third-order or higher) and often employ some form of limiting (Shchepetkin and McWilliams, 1998; Quartapelle, 1998; Warburton et al., 1998; Ezer et al., 2002).

The enforcement of the aforementioned properties in traditional finite element oceanic models is more complicated due to the unstructured nature of the grids and the Galerkin formulation. Upstream-biased

* Corresponding author. Tel.: +1 732 932 6555.
E-mail addresses: julia@imcs.rutgers.edu (J.C. Levin), miskandarani@rsmas.miami.edu (M. Iskandarani), dale@imcs.rutgers.edu (D.B. Haidvogel).

1463-5003/$ - see front matter
doi:10.1016/j.ocemod.2005.10.001

finite-element schemes have commonly relied on stabilization methods (Brooks and Hughes, 1982; Hughes et al., 1989), but they incur a substantial computational cost, particularly for large simulations, as unsymmetric systems of algebraic equations must be solved at every time step. The Discontinuous Galerkin Method (DGM, see Cockburn, 1998; Warburton et al., 1999 and references therein for more details) offers a more natural setting in which to achieve the same aims while avoiding the inversion of big linear systems. DGM's advantages include: upstream-biased fluxes at element edges, enforcement of local conservation, and element-wise (independent) calculations of a discontinuously represented solution.

The success of DGM in simulating advection-dominated flows has prompted us to re-examine the solution algorithms within the spectral element ocean model (SEOM) (Iskandarani et al., 2003), particularly those concerned with the temperature and salt evolution equations. These equations are of the advection–diffusion type and are characterized by a very high Peclet number. The SEOM algorithms have thus far relied on the classical spectral element formulation; their behavior mimics that of high-order centered-difference schemes whereby unresolved frontal structures lead to numerical noise in the form of Gibbs oscillations, and to numerical instabilities. The C^0 continuity requirement is a further burden particularly in the presence of small-scale topography.

The present article focuses on assessing the benefits of DGM-based advection scheme for oceanic simulations. The emphasis is on improving the advection schemes currently used in SEOM, and on enhancing model robustness in under-resolved circumstances. Note that the DGM formulation adopted here can be described as a hybrid, since the momentum equations are still formulated using the traditional continuous Galerkin method (CGM). Oliger and Sundstrom (1978) and Browning and Kreiss (1986) show that the Riemann problem is ill-posed for inviscid hydrostatic primitive equations in a sence that it is impossible to find a unique set of characteristic directions on open boundaries. This leads to a difficulty in solving the Riemann problem on any element edge, making the full DGM approach problematic. Our formulation avoids this difficulty by applying the DGM to the pressure and tracer fields only. This formulation is also substantially cheaper than the full DGM, since the approximate Riemann solvers used in the latter are usually expensive. The DGM reformulation of the tracer evolution equations raises the issue of the proper treatment of the baroclinic pressure gradient term: the discontinuous tracers yield a discontinuous density and a discontinuous hydrostatic pressure. A similar consideration holds for the barotropic pressure if the sea surface height is also treated via DGM. A simple weak formulation of these pressure gradient terms is sufficient to evaluate these terms stably. Furthermore, spurious pressure mode are avoided by simply reducing the polynomial degree for the pressure by two as was done in Iskandarani et al. (1995).

The present article is structured as follows: Section 2 presents the CG and DG formulations for the shallow water equations. The new formulation is validated against several two-dimensional test problems in Section 3, Comparison between CGM and DGM is presented for a solution with a shock (Section 3.2); and for an unforced smooth solution with a planetary vorticity gradient (Section 3.1). Comparison of different strategies for stabilizing under-resolved simulations for both CGM and DGM is presented in Section 3.3. The new three-dimensional formulation is then presented in Section 4, and its performance is compared to that of the continuous Galerkin method in Section 4.1 for steep slope 3D simulation.

2. CGM and DGM for the shallow water equations

2.1. The shallow water equations (SWE)

The SWE are obtained by vertical integration of the three-dimensional Navier–Stokes equations along with the assumptions of hydrostatic pressure and a vertically uniform horizontal velocity profile. Let Ω be the two-dimensional region occupied by the fluid and let Γ denote its boundary. The reduced gravity SWE in Ω are given by the continuity and momentum equations:

$$\frac{\partial \zeta}{\partial t} + \nabla \cdot [h\mathbf{u}] = 0, \tag{1}$$

$$\frac{\partial \mathbf{u}}{\partial t} + \mathbf{u} \cdot \nabla \mathbf{u} + \mathbf{f} \times \mathbf{u} = \frac{\vec{\tau}}{\rho h} - g' \nabla \zeta - \gamma \mathbf{u} + \frac{\nabla \cdot [\nu h \nabla \mathbf{u}]}{h}, \tag{2}$$

where $\mathbf{u} = (u, v)$ is the horizontal velocity vector; $h = H + \zeta$ the fluid thickness; H, the resting depth of the fluid; ζ, the free surface elevation; $\mathbf{f}$, the vertical component of the Coriolis force; $g' = \Delta\rho g/\rho_0$, the reduced gravity; γ, the bottom drag coefficient; ν, the lateral viscosity coefficient; $\vec{\tau} = (\tau_x, \tau_y)$ the wind stress acting on the surface of the fluid; and, ∇, the two-dimensional gradient operator. A concise discussion of the energetically consistent form of the shallow water equations is given in Gent (1993).

The boundary conditions are Dirichlet conditions on $\mathbf{u}$ and/or ζ:

$$\zeta = \zeta^b \text{ on } \Gamma_{\mathrm{D}}^{\zeta}, \quad \mathbf{u} = \mathbf{u}^b \text{ on } \Gamma_{\mathrm{D}} \tag{3}$$

to specify the flow at the boundary and Neumann conditions on $\mathbf{u}$:

$$\nu\nabla\mathbf{u}\cdot\mathbf{n} = \mathbf{q} \text{ on } \Gamma_{\mathrm{N}} \tag{4}$$

to specify the stresses, where Γ_{D} and Γ_{N} are the boundaries where the Dirichlet and Neumann conditions are applied, respectively. Further details on the appropriate boundary conditions are given in Bernardi and Pironneau (1991).

2.2. Galerkin formulations

The starting point of the spectral element ocean model is the Galerkin formulation of the shallow water equations:

$$\int_A \frac{\partial\zeta}{\partial t} w^p \,\mathrm{d}A = -\int_A \{\nabla\cdot[h\mathbf{u}]\} w^p \,\mathrm{d}A, \tag{5}$$

$$\int_A \frac{\partial\mathbf{u}}{\partial t} w \,\mathrm{d}A = \int_A \left\{\frac{\vec{\tau}}{\rho h} - \mathbf{u}\cdot\nabla\mathbf{u} - \mathbf{f}\times\mathbf{u} - g'\nabla\zeta - \gamma\mathbf{u} + \frac{\nu\nabla h\cdot\nabla\mathbf{u}}{h}\right\} w \,\mathrm{d}A - \int_A \nu\nabla\mathbf{u}\cdot\nabla w \,\mathrm{d}A + \oint_{\Gamma_{\mathrm{N}}} \mathbf{q} w \,\mathrm{d}S, \tag{6}$$

where w^p and w are the basis functions associated with the surface elevation and the velocity, respectively.

The spatial discretization proceeds by subdividing the domain into a set of conforming quadrilateral isoparametric elements. Each element is mapped into the unit square in the computational domain (ξ, η), and the variables ζ and $\mathbf{u}$ are interpolated as

$$\begin{cases} \zeta(\xi,\eta) = \sum_{i=1}^{N^p}\sum_{j=1}^{N^p} \zeta_{i,j}(t) h_i^p(\xi) h_j^p(\eta), \\ \mathbf{u}(\xi,\eta) = \sum_{i=1}^{N^v}\sum_{j=1}^{N^v} \mathbf{u}_{i,j}(t) h_i^v(\xi) h_j^v(\eta), \end{cases} \tag{7}$$

where $\zeta_{i,j}$ is the surface elevation at the pressure collocation nodes $(\xi_{i,j}^p, \eta_{i,j}^p)$, $(i,j) = 1,\ldots,N^p$, and $\mathbf{u}_{i,j}$ is the velocity vector at the velocity collocation nodes $(\xi_{i,j}^v, \eta_{i,j}^v)(i,j) = 1,\ldots,N^v$. N^p and N^v are the number of nodes per element in the ξ and η directions for the pressure and velocity interpolation, respectively. In order to avoid spurious pressure modes in the incompressible limit, in both the continuous Galerkin and the discontinuous Galerkin formulations, a staggered mesh is employed where the order of the pressure interpolation is two less than the velocity (Iskandarani et al., 1995), therefore $N^p = N^v - 2$.

The velocity basis functions h_i^v for the CGM and DGM formulations are the Gauss–Lobatto–Legendre cardinal functions (Boyd, 2001):

$$h_i^v(\xi) = \frac{-(1-\xi^2)L'_{N^v-1}(\xi)}{N^v(N^v-1)L_{N^v-1}(\xi_i^v)(\xi-\xi_i^v)}, \quad i = 1,2,\ldots,N^v. \tag{8}$$

L_{N^v-1} denotes the Legendre polynomial of degree $(N^v - 1)$ and L'_{N^v-1} denotes its derivative. The ξ_i^v are the N^v Gauss–Lobatto–Legendre points, i.e. they are roots of the function $(1-\xi^2)L'_{N^v-1}$. The pressure interpolation functions h_i^p for CGM are defined similarly but with the superscript v replaced by p.

The discontinuous formulation differs from the continuous by the choice of collocation points and basis functions for the pressure, while keeping the velocity definition the same. For the pressure, instead of using a Gauss–Lobatto–Legendre grid, a Gauss–Legendre grid is used. This grid is easier to use in upwind schemes

than the Gauss–Lobatto–Legendre grid, as it does not have collocation points at the element corner points for which computing normal fluxes is problematic: at corner point no unique normal direction can be specified. The collocation points for the pressure ξ_i^p are the roots of the Legendre polynomial L_{N^p}. The corresponding basis functions are Gauss–Legendre cardinal functions:

$$h_i^p(\xi) = \frac{L_{N^p}(\xi)}{L'_{Np}(\xi_i^p)(\xi - \xi_i^p)}, \quad i = 1, 2, \ldots, N^p. \tag{9}$$

In the CGM and DGM, a system of ordinary differential equations (for ζ and $\mathbf{u}$) is obtained after inserting (7) into (5) and (6), and substituting $h_i^p h_i^p$ for w^p and $h_i^v h_j^v$ for w:

$$M^p \frac{\mathrm{d}\zeta}{\mathrm{d}t} = c, \tag{10}$$

$$M^v \frac{\mathrm{d}\mathbf{u}}{\mathrm{d}t} = \mathbf{a}. \tag{11}$$

The matrices M^p and M^v are the mass matrices associated with the pressure and velocity interpolation functions, respectively; they are defined as

$$M^p_{ij,kl} = \int_A h_i^p(\xi) h_j^p(\eta) h_k^p(\xi) h_l^p(\eta)\,\mathrm{d}A = \int_A w_{ij}^p w_{kl}^p\,\mathrm{d}A, \tag{12}$$

$$M^v_{ij,kl} = \int_A h_i^v(\xi) h_j^v(\eta) h_k^v(\xi) h_l^v(\eta)\,\mathrm{d}A = \int_A w_{ij} w_{kl}\,\mathrm{d}A. \tag{13}$$

In the CGM, the right hand side vectors are:

$$\mathbf{a}_{ij} = \int_A \left\{ \frac{\vec{\tau}}{\rho h} - \mathbf{u}\cdot\nabla\mathbf{u} - \mathbf{f}\times\mathbf{u} - g'\nabla\zeta - \gamma\mathbf{u} + \frac{\nu\nabla h\cdot\nabla\mathbf{u}}{h} \right\} w_{ij}\,\mathrm{d}A - \int_A \nu\nabla\mathbf{u}\cdot\nabla w_{ij}\,\mathrm{d}A + \oint_{\Gamma_N} w_{ij}\mathbf{q}\,\mathrm{d}S, \tag{14}$$

$$c_{ij} = -\int_A \{\nabla\cdot[h\mathbf{u}]\} w_{ij}^p\,\mathrm{d}A. \tag{15}$$

Eqs. (10) and (11) hold at the elemental level. The assembly procedure adds the contribution of the different elements to the system of equations.

In the DGM formulation, since all the pressure collocation points are located inside each element, no continuity of pressure is imposed across element edges. Since ζ is discontinuous, strong forms of the Galerkin formulation of the pressure gradient and horizontal divergence cannot be used; the gradient of the pressure does not exist on the element edges. Instead, a weak form of the two operators is used. For each element E, the weak form of the pressure gradient operator is

$$\int_E g\zeta\nabla w\,\mathrm{d}A - \oint_{\delta E} g\zeta\mathbf{n}w\,\mathrm{d}S. \tag{16}$$

The weak form of the horizontal divergence operator is

$$\int_E h\mathbf{u}\cdot\nabla w^p\,\mathrm{d}A - \oint_{\delta E} h\mathbf{u}\cdot\mathbf{n}w^p\,\mathrm{d}S, \tag{17}$$

where δE is the boundary of an element E, and $\mathbf{n}$ is the normal direction to that boundary.

By the definition of the Gauss–Lobatto Cardinal functions,

$$h_i^v(\xi_j^v) = \delta_{ij} \quad \forall i \neq j, \tag{18}$$

where δ_{ij} is a Kronecker delta function. Thus the boundary integral in (16) vanishes for all test functions w that correspond to the internal points ($\xi_i^v \neq \pm 1$). For those w that correspond to the edges, the elemental contributions are assembled together. Since approximations of ζ on two neighboring elements are close to each other, and unit vectors $\mathbf{n}$ have opposite directions for the two elements, the boundary integrals in (16) cancel each other during the elemental assembly.

The Gauss–Legendre Cardinal functions h^p that are used in the divergence operator (17) have the same property as (18), but there are no collocation points on the edges. All functions h^p_{ij} are not zero on the element edges. Thus the boundary integral does not vanish. There are different ways to compute the numerical flux $(h+\zeta)\mathbf{u}\cdot\mathbf{n}$ on the edge (Cockburn, 1998). We choose a more diffusive upwind-biased numerical flux; an upstream element is used to compute the flux, and then this flux is used in boundary integrals in both neighboring elements.

Similar to the CGM formulation, the diffusion term is split into two parts. The term $\nabla\cdot(\nu\nabla u)$ is straightforward and is discretised using the weak formulation. The second term $\nu/h\nabla h\cdot\nabla u$ which is similar to an advection of a continuous field by a discontinuous field is difficult to discretize consistently: it is done by simple averaging of the elemental contributions.

Replacing the corresponding strong operators in (14) and (15) by the weak operators (16) and (17), we obtain the right hand side vectors for the DGM formulation

$$\mathbf{a}_{ij} = \int_A \left\{\frac{\vec{\tau}}{\rho h} - \mathbf{u}\cdot\nabla\mathbf{u} - \mathbf{f}\times\mathbf{u} - \gamma\mathbf{u} + \frac{\nu\nabla h\cdot\nabla\mathbf{u}}{h}\right\} w_{ij}\,\mathrm{d}A - \int_A \nu\nabla\mathbf{u}\cdot\nabla w_{ij}\,\mathrm{d}A + \int_A g'\zeta\nabla w_{ij}\,\mathrm{d}A + \oint_{\Gamma_N} w_{ij}\mathbf{q}\,\mathrm{d}S,$$

$$c_{ij} = \int_A h\mathbf{u}\cdot\nabla w^p_{ij}\,\mathrm{d}A - \oint_{\delta A} Q w^p_{ij}\,\mathrm{d}S, \tag{19}$$

where δA are all the element edges, and Q is the upwind flux at the element edge:

$$Q = \frac{\mathbf{u}\cdot\mathbf{n} + |\mathbf{u}\cdot\mathbf{n}|}{2} h^+ + \frac{\mathbf{u}\cdot\mathbf{n} - |\mathbf{u}\cdot\mathbf{n}|}{2} h^-, \tag{20}$$

where h^+ and h^- refer to the layer thickness at element edges as estimated from data within element E and its edge-neighbor, respectively (see Cockburn, 1998; Karniadakis and Sherwin, 1999 for more details).

Note that even an explicit time integration scheme requires the inversion of the matrices M^v and M^p. Fortunately, the mass matrices can be made diagonal by evaluating the integrals with Gauss–Lobatto quadrature of order N^v (Abramowitz and Stegun, 1964), to compute the left hand side in the discretised momentum equations; Gauss–Lobatto and Gauss quadratures of order N^p are used to evaluate the left hand sides in the CGM and DGM forms of the continuity equation, respectively. The diagonal form of the mass matrices leads to tremendous savings in computations and storage with negligible loss of accuracy.

2.3. Time integration of equations

The explicit time integration of Eqs. (10) and (11) may be performed with (e.g.) a third-order Adams–Bashforth (AB3) scheme. Each of the equations in (10) and (11) can be written in the generic form $M\,\mathrm{d}u/\mathrm{d}t = r$ where u and r are the vector of unknowns and the vector of right hand sides, respectively, and M is one of the mass matrices. The AB3 scheme takes the form [see Gear, 1971 for example]:

$$u^{n+1} = u^n + \Delta t M^{-1}\left[\frac{23}{12}r^n - \frac{16}{12}r^{n-1} + \frac{5}{12}r^{n-2}\right]. \tag{21}$$

The calculations require information at two previous time levels and thus a start-up method is needed at the initial timestep; we choose a fourth-order Runge–Kutta scheme. All computations are performed at the elemental level and only the vector r needs to be assembled at each timestep.

3. Two-dimensional numerical tests

The performance of the DG formulation presented in the previous section is documented using numerical experiments of varying degree of difficulty. We first validate the DG formulation for smooth problems where the CG and DG formulations are expected to behave similarly. We then investigate the advantages of using DG for under-resolved problems. Two sample experiments are presented. The first features a strong shock that cannot be resolved (for the inviscid case) even under mesh refinement, while the second involves an

under-resolved meandering jet. We also investigate various mechanisms to control Gibbs oscillations and report on their effectiveness for the DG formulation.

3.1. Propagation of monopole vortex on a β-plane

Here, we simulate the propagation and the boundary-reflection of a monopole vortex on a β-plane using the hybrid discontinuous formulation and the traditional continuous formulation. The aim is to validate the DG solution against the CG one for the case of a smooth and resolved solution. The basin size is 3600×2800 km^2 and has a uniform depth of 1000 m. The model is run in reduced gravity mode to simulate the dynamics of the first baroclinic mode. The physical parameters are: $g' = 0.081$ m^2/s; the Coriolis parameter is $f = 9 \times 10^5 + 1.8 \times 10^{-11}(y - L/2)$ where y is the distance in meters from the southern boundary and L is the meridional size of the basin; and the viscosity is set to 100 m^2/s. The basin is divided into 10×8 elements with $N^v = 10$ and $N^p = 8$. The elements are refined around the coastal wave guide and in the western boundary region to resolve the western boundary current and the short waves arising from the reflection of Rossby waves. The time step is 57.6 s. The simulation is started with an initial monopole vortex in gradient balance as in Iskandarani et al. (1995). Fig. 1 compares the continuous spectral element solution and the DGM-based formulation. The two formulations yield similar interface height (pressure) patterns. Note in particular that

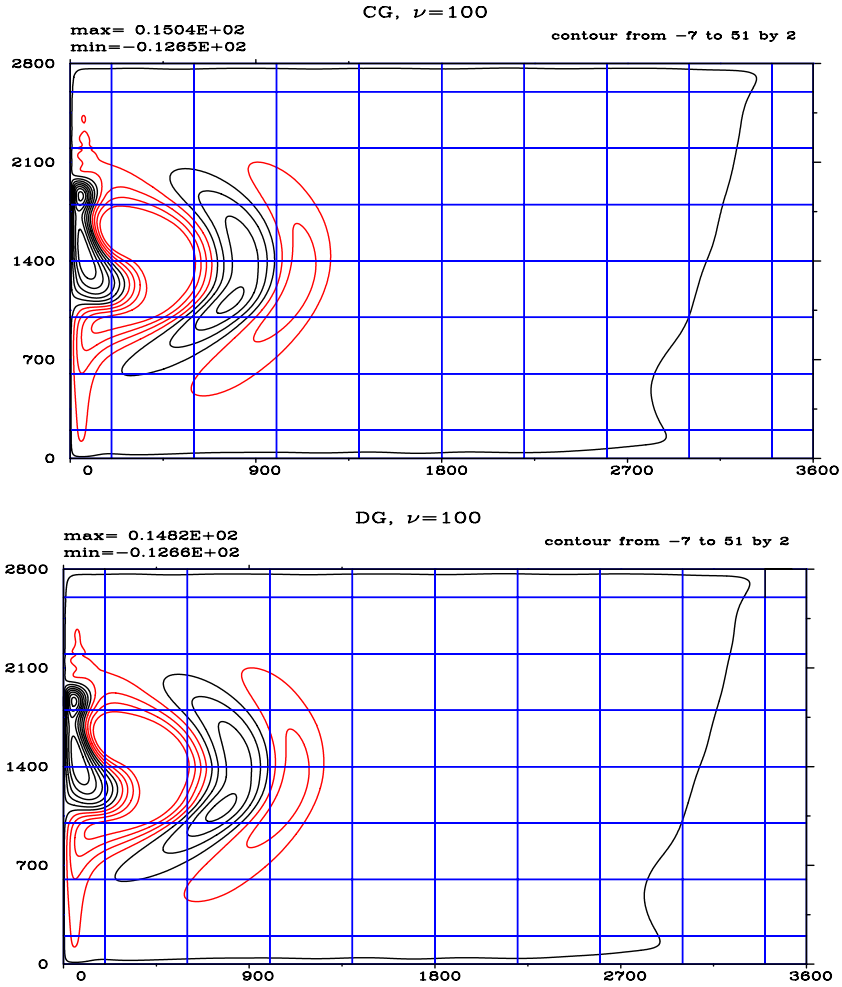

Fig. 1. Interface height contours at day 200 of the CGM (top) and DGM (bottom) solutions for the monopole vortex problem. The elemental grid is shown. Red contours are negative.

the phase speeds and amplitudes of the different waves are very similar in both simulations; the peak detected in the CGM solution is somewhat higher then in the DGM one but that could be attributed to the different distribution of pressure points in the two models.

3.2. Supercritical flow in a channel

Here, we simulate the hydraulic jump formed when a supercritical flow in a channel encounters a sudden change in channel cross-section as depicted in Fig. 2. The equations solved are the nonlinear shallow water equations without drag, Coriolis, or wind stress. The inflow at the left boundary is specified as $u_0 = 8.57$ m/s and the water column depth $h_0 = 1$ m; these parameters correspond to a Froude number $Fr = 2.74$. For a channel-deflection angle of 8.95°, the analytical solution predicts an angle of 30° between the shock line and the channel wall, and downstream values of water depth, velocity and Froude number of $H_d = 1.5$ m, $u_d = 7.9556$ m/s, and $Fr = 2.075$, respectively (Alcrudo and Garcia-Navarro, 1993; Choi et al., 2004). The boundary conditions are free-slip on the side walls; no conditions are required on the outflow. The initial condition is a uniform flow: $u = u_0$, $v = 0$, $h = h_0$. The equations are integrated in time until a steady state is achieved.

We investigate the convergence of the DG and CG formulations to the (in-viscid) analytical solution using h- and p-refinements. Viscous dissipation was used to control the amplitude of the Gibbs oscillations around the hydraulic jump. The viscosity level was chosen to be the minimum needed to prevent oscillations on the coarsest grid. This value was then scaled down by the square of the average resolution for the finer grids, so that the viscous time scale is the same on all grids. Various metrics were computed after 20 s of simulation time, and the results are listed in Table 1. The average downstream values of velocity and Froude number were computed in a region that excluded the channel boundary and the hydraulic jump. For comparison we also show the results of a standard CGM formulation. Our DGM-based method is superior to CGM in terms of the magnitude of overshoots and undershoots. Slow convergence of the average downstream velocity and Froude number is achieved with DGM, while no convergence is obtained with CGM.

Fig. 3 compares the free surface elevations obtained with the DGM-based formulation and the standard CGM formulation in the four p-refinement experiments. Both methods display similar diffusion of the hydraulic jump on the coarse grids due to the large viscosity used; the width of the jump decreases as the grid is refined and viscosity is reduced. The figure shows that the CGM results show significant oscillations upstream of the hydraulic jump, especially in cases with low viscosity. In the DGM results the upstream oscillations are negligible.

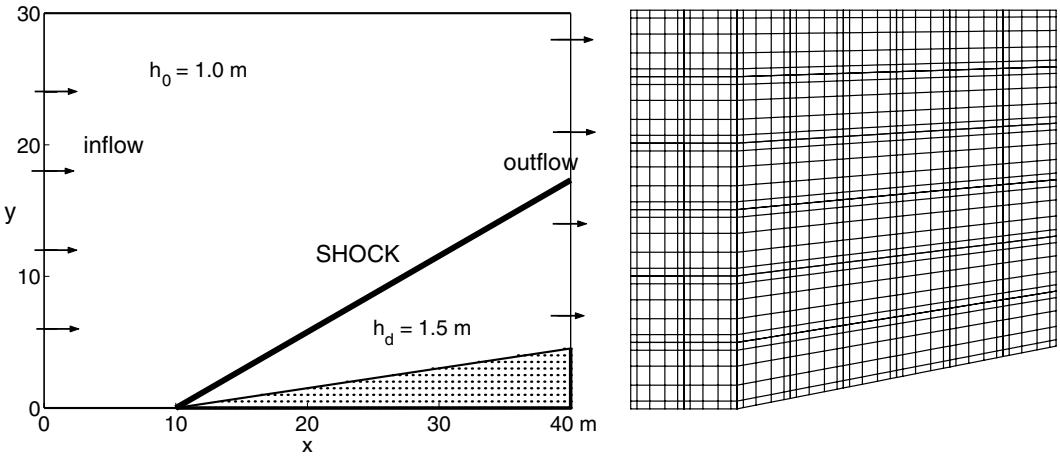

Fig. 2. The left panel shows a schematic of the supercritical channel flow test problem; the channel-deflection angle is 8.95°. The right panel shows the spectral element grid with 6×6 collocation points in each element. The other grids are obtained by either p- or h-refinement.

Table 1
Comparison of metrics obtained on grids of various resolution (h and p-refinement) using CGM and DGM methods

K	N	v	DGM				CGM			
			ζ_{max}	ζ_{min}	$\|u\|$	$\|Fr\|$	ζ_{max}	ζ_{min}	$\|u\|$	$\|Fr\|$
4×3	6	9.60	0.455	−0.002	8.295	2.280	0.512	−0.062	8.243	2.230
8×6	6	2.40	0.501	−0.010	8.130	2.170	0.623	−0.068	7.633	2.024
12×9	6	1.10	0.485	−0.013	8.060	2.133	0.725	−0.061	8.578	2.210
16×12	6	0.60	0.492	−0.017	8.011	2.114	0.468	−0.107	7.259	1.024
8×6	6	2.40	0.500	−0.009	8.130	2.170	0.623	−0.068	7.633	2.024
8×6	8	1.20	0.470	−0.010	8.068	2.137	0.469	−0.099	7.381	1.955
8×6	12	0.50	0.470	−0.010	7.998	2.109	0.470	−0.110	7.341	1.941
8×6	16	0.25	0.470	−0.011	7.955	2.097	0.470	−0.115	7.379	1.949
Exact			0.500	0.000	7.9556	2.075	0.500	0.000	7.9556	2.075

N is the number of collocation points in each element; v is the harmonic viscosity in m^2/s; (ζ_{max}, ζ_{min}) (m) are the maximum and minimum value of free surface elevation respectively, $\zeta = h - 1$ m; $|u|$ is the average u-velocity below the shock in (m/s), $|Fr|$ is the average Froude number below the shock.

3.3. Test case: Wind-driven circulation in a basin

Here the hybrid discontinuous model is applied in the reduced gravity mode to the canonical problem of a wind-driven, double-gyre, mid-latitude ocean in a rectangular basin (Haidvogel et al., 1992; Holland, 1978; McCalpin and Haidvogel, 1996). The problem is solved in a basin of 3600×2800 km and has free-slip boundary conditions. The depth of the active layer is $h = 600$ m and the reduced gravity $g' = 0.02$ m/s^2. The Coriolis parameter in the mid-latitude β-plane approximation has the form:

$$f = f_0 + \beta(y - y_0), \tag{22}$$

where $f_0 = 7.27\times10^{-5}$ 1/s, $\beta = 1.97\times10^{-11}$ 1/(ms), and $y_0 = 1400$ km.

The flow starts from rest. The circulation is forced by a steady zonal wind, which is similar to that of McCalpin and Haidvogel (1996) and has the form:

$$\tau_x = \tau_0\left\{(1 + 4\alpha(y/L - 1/2))\cos(2\pi y/L) - \frac{4\alpha}{2\pi}\sin(2\pi y/L)\right\}, \tag{23}$$

where $\tau_0 = -5\times10^5$ (m/s)^2, $\alpha = 0.13$, $L = 2800$ km. The wind stress component in the meridional direction τ_y is set to zero. The wind forcing is chosen in order to produce a free jet analogous to the Gulf Stream (McCalpin and Haidvogel, 1996). The wind stress (23) has zero curl at the northern and southern boundaries. A bottom drag $\gamma = 1\times10^7$ 1/s is used to balance the wind stress forcing. The viscosity $v = 120$ m^2/s is kept small enough to avoid dissipating the jet and the eddies. With this set of parameters, the Rossby radius is $R = \sqrt{g'h}/f_0 = 48$ km at the central latitude, and the Munk layer thickness is $d = (v/\beta)^{1/3} = 18$ km.

The grid is uniform in the meridional direction and slightly nonuniform zonally: the resolution is enhanced near the western boundary. Spectral expansions of 7×7 and 5×5 are used in all elements for the velocity and pressure grids, respectively. The time step is 450 s. The grid has an average resolution of 26 km, and does not resolve the meandering jet. Additional dissipation mechanisms are hence required to prevent small-scale nonlinear instabilities from destroying the solution. We tested two different strategies: an adaptive slope limiter designed to prevent the generation of spurious extrema, and a spectral filter designed to dissipate quickly the amplitude of the high wavenumbers in the solution. The first strategy is suitable for the DG formulation only whereas the second can be applied to either one.

Slope limiting was first proposed by Cockburn and Shu (1989); Cockburn et al. (1989) for linear elements, $N = 1$, to eliminate Gibbs oscillations from DGM calculations. Their scheme limits the slope of the interpolation polynomial within an element in comparison with those implied by the variation of the solution-mean across elements. The higher order Legendre coefficients, if any, are set to zero when the limiter is activated. Biswas et al. (1994) extended the linear-element limiter to high-order elements without resorting to the drastic

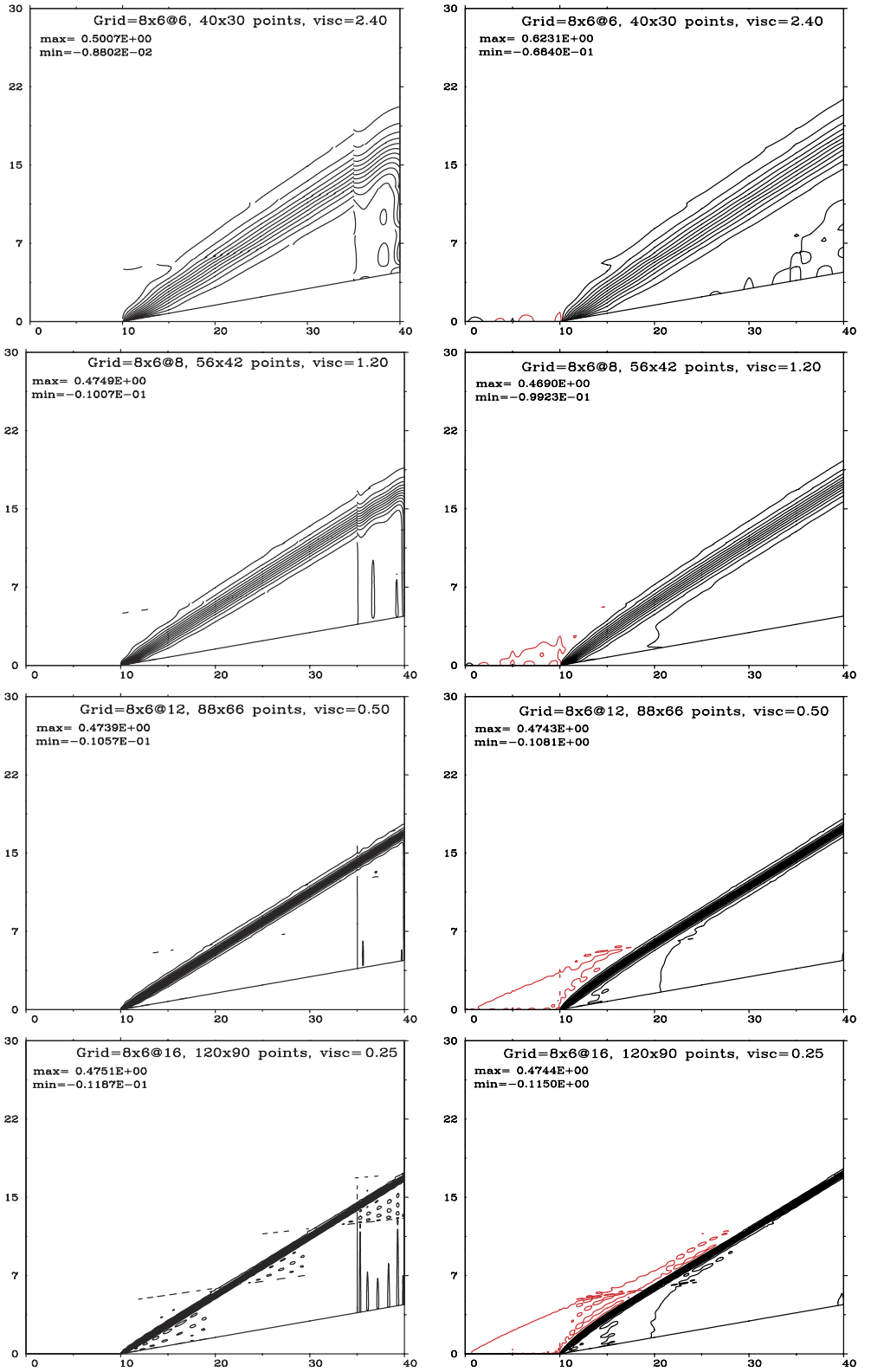

Fig. 3. Contours of free surface elevation with *p*-refinement for DGM (left column) and CGM (right column) formulations. The polynomial degree of velocity is, from top to bottom, 5, 7, 11 and 15, respectively, on an 8×6 elemental partition of the domain.

step of setting to zero all high-order coefficients. They suggested limiting the derivatives of the solution, starting with the highest order one, according to

$$(2k+1)\tilde{C}_{k+1,e} = \text{minmod}\,\{(2k+1)C_{k+1,e}, C_{k,e} - C_{k,e-1}, C_{k,e+1} - C_{k,e}\},$$

where the minmod function is defined as follow:

$$\text{minmod}(a,b,c) = \begin{cases} \text{sgn}(a)\,\min(|a|,|b|,|c|), & a,b,c \text{ have same sign} \\ 0 & \text{otherwise} \end{cases}$$

and where $C_{n,e}$ is the Legendre spectral coefficient of degree n in element e. The limiter is applied first to the highest-order coefficient $C_{N,e}$. The process stops if no modification takes place; otherwise the next highest coefficient is limited. This "gradual" application of the slope limiter is meant to preserve accuracy when the solution is smooth. The resulting coefficients $\tilde{C}_{n,e}$ are then used to obtain a "limited" solution: $\tilde{T}_e(\xi) = \sum_{n=0}^{N} \tilde{C}_{n,e} L_n(\xi)$. In our tests the slope limiter of Biswas et al. (1994) is applied to the free surface elevation.

Fig. 4(b) shows the results of the slope-limited DG simulation. The solution is excessively diffused: the jet is wide, and eddy production is inhibited. Biswas et al. (1994) used their slope limiter in an adaptive setting using lower order elements, whereas the present problem uses a relatively small number of high-order elements. The diffusive solution is indicative of an "over-active" slope limiter that limits all the high-order coefficients within each element, and effectively lowering the degree of the interpolation polynomial. The situation is made worse by the large-size of the elements. We thus find that the slope limiter is not effective for unresolved or marginally resolved flows; moreover, in higher order elements it is not scale selective enough. This result is in agreement with the test that we performed on the slope limiter in Iskandarani et al. (2005).

We then compare the effect of the slope limiter to that of the vorticity-divergence filter of Levin et al. (1997). This filter is a modification of the classical spectral filters which damp small-scale numerical noise in spectral space without affecting the resolved large-scale structure. The filter is applied to the vorticity and divergence fields associated with the velocity; a C^0-continuous filtered velocity fields is then reconstructed from the filtered quantities by solving a couple of elliptic equations for the velocity components. The vorticity-divergence filter was designed to allow the independent application of the filter within each element while maintaining the continuity of the solution, and the imposed boundary conditions on element boundaries. The strength of the dissipation is determined by several parameters which include, the cut-off wavenumber, the strength of the filter, and the frequency of application.

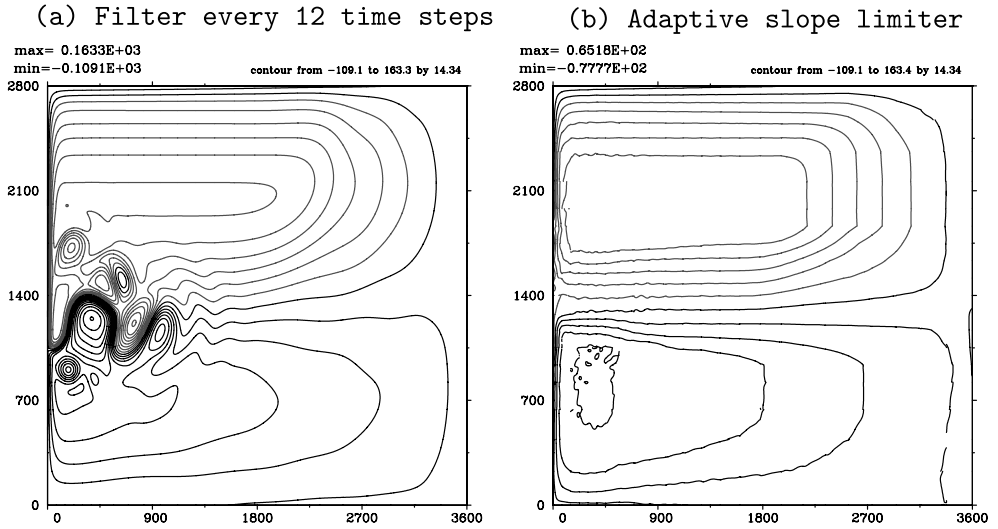

Fig. 4. Contours of surface height for a double gyre problem obtained with a discontinuous shallow water model. Light contours are negative.

Fig. 4(a) shows the results of the simulations with the vorticity-divergence filter. The filter is applied every 12 time steps to the three highest wavenumbers only (amplitudes corresponding to the three highest wave numbers are multiplied by 0.95, 0.81 and 0.61, respectively). The solution is superior to that with the slope limiter. The simulation produces a double gyre and a turbulent mid-latitude jet. The separation point of the jet oscillates widely, and the strong meandering of the jet leads to the formation of rings.

Similar double-gyre experiments were done in Levin et al. (1997) using the continuous formulation where the same filtering strategy was applied to kill the small-scale nonlinear instability. The new discontinuous model requires less frequent filtering for stabilization, and produces a result with a 4% bigger mean kinetic energy. Without the filter, both continuous and discontinuous simulations fail at approximately the same time.

4. CGM and DGM for the tracers

The CGM and DGM formulation for the three-dimensional hydrostatic equations is summarized in this section. The governing equations are presented in Iskandarani et al. (2003) and include two horizontal momentum equations for the velocity and two advection–diffusion equations for the salt and temperature tracers. The vertical momentum equation is reduced to a simple balance between the vertical pressure gradient and the buoyancy force; the latter is computed by integrating the density from the surface. The continuity equation is used to compute the vertical velocity. Barotropic pressure and velocity are obtained by vertically averaging the momentum and continuity equations; they are solved by the method described in Section 2. The traditional continuous spectral element formulation for the tracer evolution has the form

$$\int_E \frac{\partial T}{\partial t}\psi \,\mathrm{d}V = -\int_E \mathbf{u}\cdot\nabla T\psi \,\mathrm{d}V - \int_E \nu\nabla T\cdot\nabla\psi \,\mathrm{d}V, \tag{24}$$

where ψ is a three-dimensional basis function, which is a tensor-product of three one-dimensional Legendre Gauss–Lobatto Cardinal functions of the form (8).

The tracer evolution equation has been changed in the DGM formulation. Discontinuous basis functions ψ are used in a discretization of tracers. Upstream-biased advective flux (Cockburn, 1998), similar to the one described in Section 2 is applied; and the diffusive flux is computed according to the scheme proposed by Cockburn and Shu (1998). In this scheme, the diffusive operator is split into a system of two first-order equations, and then an estimate from an element to the left or to the right of a boundary is used alternatively to obtain a numerical flux for each of the two first-order operators. The details of the formulation can be found in Cockburn (1998); Cockburn and Shu (1998); Karniadakis and Sherwin (1999).

The DGM form of the tracer equation is:

$$\int_E \frac{\partial T}{\partial t}\psi \,\mathrm{d}V = \int_E T\mathbf{u}\cdot\nabla\psi \,\mathrm{d}V - \int_E \nu\mathbf{T}^{(\nabla)}\cdot\nabla\psi \,\mathrm{d}V - \oint_{\partial E} Q^T\psi \,\mathrm{d}s + \oint_{\partial E} \nu\mathbf{T}^{(\nabla)^+}\cdot\mathbf{n}\psi \,\mathrm{d}s, \tag{25}$$

where Q^T is the upstream-biased advective flux

$$Q^T = \frac{\mathbf{u}\cdot\mathbf{n} + |\mathbf{u}\cdot\mathbf{n}|}{2}T^+ + \frac{\mathbf{u}\cdot\mathbf{n} - |\mathbf{u}\cdot\mathbf{n}|}{2}T^-; \tag{26}$$

ψ is a three-dimensional basis function, which is a tensor-product of Legendre–Gauss cardinal functions of the form (9); A^+ and A^- denote the values of A to the right or to the left of an edge, respectively; and $\mathbf{T}^{(\nabla)}$ denotes a gradient of T: $\mathbf{T}^{(\nabla)} = \nabla T$. It is computed from the following auxiliary equation:

$$\int_E \mathbf{T}^{(\nabla)}\psi \,\mathrm{d}V = -\int_E T\nabla\psi \,\mathrm{d}V + \oint_{\partial E} T^-\mathbf{n}\psi \,\mathrm{d}s. \tag{27}$$

The sole modification to the momentum equations is the adoption of the weak form of the baroclinic pressure gradient term as the latter is now discontinuous. The Gauss–Lobatto quadrature of order N^v is used to ensure the accuracy of numerical integration of the baroclinic pressure gradient term, and the upwind value of pressure is used at the edges between elements. The resulting formulation has been applied to a problem that features moving density fronts to test the model's robustness.

4.1. Gravitational overflow problem

The problem involves the gravitational adjustment of a two-density-layer system on an idealized continental shelf (Haidvogel and Beckmann, 1999). Initially, heavy fluid is located on a shelf and is separated from a lighter fluid by a vertical wall. At time zero, the vertical wall dividing the two immiscible fluids is removed; thereafter, the heavy fluid starts sliding down the slope to form a stably stratified, two-layer system. During and after the adjustment, sharp density fronts divide the two layers both horizontally and vertically.

The gravitational overflow problem is difficult because it tests the ability of the numerical model to propagate a narrow moving front. Diffusive and dispersive errors stemming from the discretization can destroy the structure of the solution quickly. The trouble manifests itself in the form of oscillations in the density field, and unphysical density extrema in the neighborhood of the front. The problem is exacerbated by the pressure gradient errors that are superimposed on the propagating fronts. A faithful model would thus eliminate the oscillations, maintain the extrema of the density fields at their initial values, and produce as narrow a front as possible.

In this experiment, the width of the domain is 200 km, the fluid depth varies from 200 m to 4000 m, and is described by the function:

$$h(x) = H_{\min} + \frac{1}{2}(H_{\max} - H_{\min})(1 + \tanh\{(x - x_0)/L_s\}),$$

where $H_{\min} = 200$ m, $H_{\max} = 4000$ m, $x_0 = 100$ km and $L_s = 10$ km.

We compare the extrema of density for the gravitational overflow problem in the continuous and in the new discontinuous formulation. In the discontinuous formulation, velocity is staggered with respect to free surface and tracers. In the continuous formulation, both velocity and tracers have the same spectral truncation. In the experiments shown, both versions have the same discretization of the velocity, but the tracer discretizations are different: discontinuous tracer discretization is two orders lower than the continuous one.

All the DGM simulations were carried out on a horizontal grid that consisted of 40 elements of order 5 for velocity, and of order 3 for tracers, so that the average velocity grid resolution was 1 km in the horizontal. In the vertical, the grid consisted of 5 elements of order 4 (a total of 21 points) for velocity; and 5 elements of order 2 (a total of 15 points) for tracers, with the resolution enhanced at the bottom. The grid is shown in Fig. 5. A time-step of 1 s was used. The simulations required a viscosity value of 1000 m^2/s to run stably. Vertical viscosity and diffusivity are set to zero. Since no reference solution is currently available for this overflow problem we confine ourselves to investigate the ability of the formulation to cope with frontal structures in the presence of steep bathymetric variations using the Gibbs oscillation as our error measure.

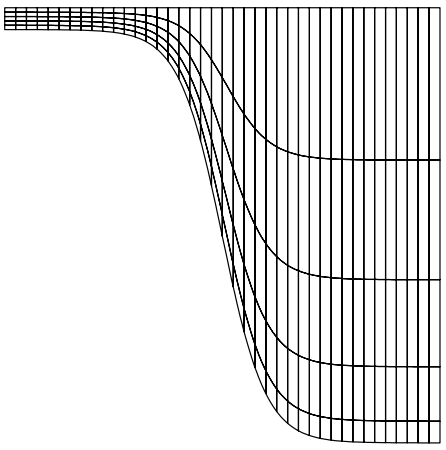

Fig. 5. Grid for the overflow problem. Only element edges are shown. The grid consists of 40 elements in the horizontal and 5 elements in the vertical. The resolution is enhanced at the bottom.

Table 2
Minima and maxima of density in sigma units

Diffusivity	CGM		DGM	
	ρ_{min}	ρ_{max}	ρ_{min}	ρ_{max}
0			−2.41	5.63
50			−1.54	5.35
100	−1.59	5.42	−1.50	5.22
500	−0.69	5.008	−1.37	5.20
1000	−0.61	4.999	−1.16	5.19

Diffusivity ranging from 0 to 1000 m^2/s. The values of density greater than 5 or less than 0 are numerically induced overshoots and undershoots, respectively. The horizontal grid spacing is 1 km. Viscosity is 1000 m^2/s.

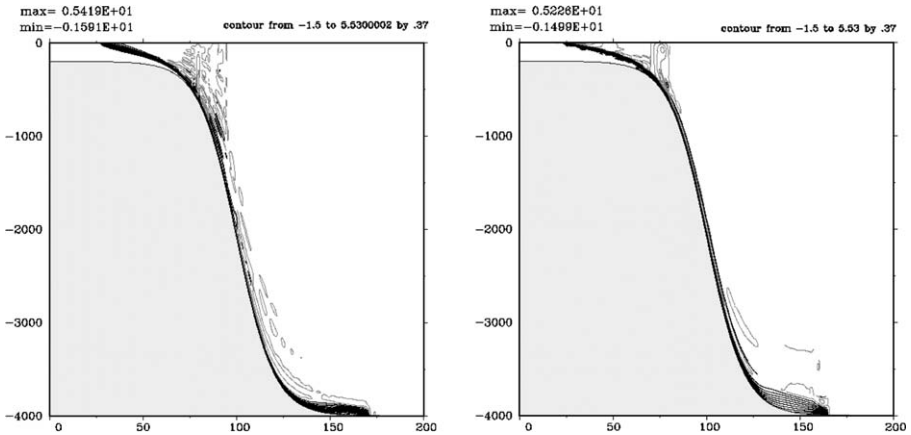

Fig. 6. Downflow of a density front along a steep slope using the continuous (left panel) and discontinuous (right panel) formulations. Dense water, initially on the shelf, flows down the slope under the influence of gravity. The density contrast between the shelf and offshore water is $\Delta\rho = 5\ kg/m^3$. The grid spacing in the horizontal is 1 km, 21 levels are used in the vertical. Viscosity is 1000 m^2/s and diffusivity is 100 m^2/s, they are applied along σ levels. The density contours are shown after 10 h of simulated time.

Comparison of the two SEOM formulation for the gravitational overflow experiment is given in Table 2. The robustness of the DGM formulation is evident: reasonable results can be obtained even in the limit of very low diffusivity where the continuous formulation fails. We note that our continuous formulation uses the same interpolation polynomial for the tracer as for the velocity; its polynomial degree is higher then that of the discontinuous formulation by 2. This leads to a bias in favor of the continuous formulation in the limit of well-resolved fronts (the high diffusivity experiments here). The transition from under-resolved to resolved occurs around a diffusivity of 500 m^2/s for the continuous formulation; the discontinuous formulation still exhibits significant unphysical oscillations in this regime. These oscillations are, nevertheless, more localized in the discontinuous formulation and remain in the neighborhood of the front. Fig. 6 compares the temperature distribution obtained with the continuous (unstaggered velocity and tracers) formulation with those of the DGM (staggered) formulation. Although the resolution of tracers is considerably lower in the DGM calculation, the errors are confined to the immediate vicinity of the density front, whereas they tend to spread and occupy a larger portion of the water column for the continuous formulation. The DGM results show a substantial reduction in the amplitude of the Gibbs oscillations produced near the front. The higher diffusivity experiments also show that the front propagation speed is sensitive to the value of the along σ-diffusivity used; larger values of diffusivity seeming to decelerate the flow.

5. Conclusion

We present a high-order finite element formulation for the solution of the shallow water equations in their two-dimensional and three-dimensional forms. The formulation uses a hybrid approach whereby the

two-dimensional continuity equation, and the tracer evolution equations are solved via a DGM formulation to take advantage of the method's nice properties for advection-dominated flows, e.g., local conservation. The momentum equations are solved via the "traditional" continuous Galerkin formulation, and the sole modification required is the weak treatment of the resulting discontinuous terms, namely the barotropic and baroclinic pressure gradient terms. The performance of the hybrid formulation was validated numerically on a number of different problems, particularly ones that features fronts and strong gradients in the flow. The new formulation is able to cope with under-resolved features better then the continuous formulation.

Acknowledgement

The present research was supported in part by ONR grant N00014-03-1-0254 and N00014-03-1-0255.

References

Abramowitz, M., Stegun, I., 1964. Handbook of Mathematical Functions, first ed. Applied Mathematics Series, Vol. 55, National Bureau of Standards, Washington, DC.

Alcrudo, F., Garcia-Navarro, P., 1993. A high-resolution Godunov-type scheme in finite volumes for the 2D shallow-water equations. International Journal for Numerical Methods in Fluids 16, 489–505.

Bernardi, C., Pironneau, O., 1991. On the shallow water equations at low Reynolds numbers. Communications in Partial Differential Equations 16 (1), 59–104.

Biswas, R., Devine, K., Flaherty, J., 1994. Parallel, adaptive finite element methods for conservation laws. Applied Numerical Mathematics 14, 255–283.

Boyd, J.P., 2001. Chebyshev and Fourier spectral methods, second ed. Dover Publications.

Brooks, A.N., Hughes, T.J.R., 1982. Streamline upwind/Petrov Galerkin formulations for convection dominated flows with particular emphasis on the the incompressible Navier–Stokes equations. Computer Methods in Applied Mechanics and Engineering 32, 199–259.

Browning, G.L., Kreiss, H.-O., 1986. Scaling and computation of smooth atmospheric motions. Tellus 38A, 295–313.

Choi, B.-J., Iskandarani, M., Levin, J., Haidvogel, D.B., 2004. A spectral finite-volume method for the shallow water equations. Monthly Weather Review 132, 1777–1791.

Cockburn, B., 1998. An introduction to the discontinuous Galerkin methods for convection dominated flows. In: Advanced Numerical Approximation of Nonlinear Hyperbolic Equations. Springer-Verlag, pp. 151–268.

Cockburn, B., Shu, C.-W., 1989. TVB Runge–Kutta local projection discontinuous Galerkin finite element method for scalar conservation laws II: General framework. Mathematics of Computations 52, 411–435.

Cockburn, B., Shu, C.-W., 1998. The local discontinuous Galerkin method for time-dependent convection–diffusion systems. SIAM Journal of Numerical Analysis 35, 2440–2463.

Cockburn, B., Lin, S.-Y., Shu, C.-W., 1989. TVB Runge–Kutta local projection discontinuous Galerkin finite element method for scalar conservation laws III: One dimensional systems. Journal of Computational Physics 84, 90–113.

Ezer, T., Arango, H.G., Shchepetkin, A.F., 2002. Developments in terrain-following ocean models: intercomparisons of numerical aspects. Ocean Modelling 4, 249–267.

Gear, C.W., 1971. Numerical Initial Value Problems in Ordinary Differential Equations. Prentice-Hall, Engelwood-Cliffs, NJ.

Gent, P., 1993. The energetically consistent shallow-water equations. Journal of the Atmospheric Sciences 50 (9), 1323–1325.

Haidvogel, D.B., Beckmann, A., 1999. Numerical Ocean Circulation Modeling. Imperial College Press.

Haidvogel, D.B., Mc Williams, J.C., Gent, P.R., 1992. Boundary current separation in a quasigeostrophic, eddy-resolving ocean circulation model. Journal of Physical Oceanography 22, 882–902.

Holland, W.R., 1978. The role of mesoscale eddies in the general circulation of the ocean—Numerical experiments using a wind-driven quasi-geostrophic model. Journal of Physical Oceanography 8, 363–392.

Hughes, T.J.R., Franca, L.P., Hulbert, G.M., 1989. A new finite element formulation for computational fluid dynamics. VIII. The Galerkin/least-square method for advective-diffusive equations. Computer Methods in Applied Mechanics and Engineering 73, 173–189.

Iskandarani, M., Haidvogel, D.B., Boyd, J.P., 1995. A staggered spectral element model with application to the oceanic shallow water equations. International Journal for Numerical Methods in Fluids 20, 393–414.

Iskandarani, M., Haidvogel, D.B., Levin, J.G., 2003. A three-dimensional spectral element model for the solution of hydrostatic primitive equations. Journal of Computational Physics 186 (2), 397–425.

Iskandarani, M., Levin, J., Choi, B.-J., Haidvogel, D.B., 2005. Comparison of advection schemes for high order hp finite element and finite volume methods. Ocean Modeling 10, 233–252.

Karniadakis, G.E., Sherwin, S.J., 1999. Spectral/hp Element Methods for CFD. Oxford University Press.

Levin, J., Iskandarani, M., Haidvogel, D.B., 1997. A spectral filtering procedure for eddy-resolving simulations with a spectral element ocean model. Journal of Computational Physics 137 (1), 130–154.

McCalpin, J.D., Haidvogel, D.B., 1996. Phenomenology of the low-frequency variability in a reduced-gravity, quasigeostrophic double-gyre model. Journal of Physical Oceanography 26 (5), 739–752.

Oliger, J., Sundstrom, A., 1978. Theoretical and practical aspects of some initial boundary value problems in fluid dynamics. SIAM Journal of Applied Mathematics 35, 419–446.

Quartapelle, L., 1998. The use of tvd limiters for forward-in-time upstream-biased advection schemes in ocean modeling. Monthly Weather Review 126 (3), 812–830.

Shchepetkin, A.F., McWilliams, J.C., 1998. Quasi-monotone advection schemes based on explicit locally adaptive dissipation. Monthly Weather Review 126, 1541–1580.

Warburton, T.C., Lomtev, L., Karniadakis, G.E., 1998. Improved advection schemes for ocean models. Journal of Atmospheric and Oceanic Technology 15 (3), 1171–1187.

Warburton, T., Lomtev, L., Karniadakis, G.E., 1999. Galerkin and discontinuous Galerkin spectral/hp methods. Computer Methods in Applied Mechanics and Engineering 175 (3), 343.

Willebrand, J., Haidvogel, D.B., 2001. Numerical ocean circulation modeling: present status and future direction. In: Church, J., Gould, J. (Eds.), Ocean Circulation and Climate. Academic Press, New York, pp. 547–556.